Effect of anion exchange ionomer content on electrode performance in AEM water electrolysis

Alaa Y. Faid [a,1,*], Lin Xie [b,1], Alejandro Oyarce Barnett [c,d], Frode Seland [a], Donald Kirk [b], Svein Sunde [a]

[a] Department of Materials Science and Engineering, Norwegian University of Science and Technology, Norway
[b] Department of Applied Chemistry and Chemical Engineering, University of Toronto, Canada
[c] SINTEF Industry, New Energy Solutions, Norway
[d] Department of Energy and Process Engineering, Norwegian University of Science and Technology, Norway

HIGHLIGHTS

- The anion exchange ionomer (AEI) content affects the electrolyzer performance.
- Cathode overpotential of Ni/C was not negligible compared to the NiO anode.
- The Ni/C cathode overpotential is more affected by AEI content than NiO anode.
- Electrode performance could be related to AEI effect on catalyst layer morphology.

ARTICLE INFO

ABSTRACT

Anion exchange membrane water electrolysis (AEMWE) has acquired substantial consideration as a cost-effective hydrogen production technology. The anion ionomer content in the catalyst layers during hydrogen and oxygen evolution reaction (HER and OER) is of ultimate significance. Herein, an in-situ half-cell analysis with reference electrodes was carried out for simultaneous potential measurements and identification of the influence of the anion exchange ionomer (AEI) content on anode and cathode performance. The measured half-cell potentials proved the influence of AEI content on the catalytic activity of HER and OER, which was supported by the rotating disk electrode (RDE) measurements. Cathode overpotential of Ni/C was not negligible and more affected by the AEI content than anode with the optimized AEI content of 10 wt% while NiO anode OER overpotential was independent of the AEI content. For the same AEI content, PGM catalysts showed higher electroactivity than Ni-based catalysts for HER and OER and the cathode catalyst's intrinsic activity is of high importance in the AEM electrolysis operation. Post-mortem analysis by SEM mapping of both AEI and catalyst distributions on the electrode surface showed the effect of AEI loading on the catalyst morphology, which could be related to the electrode performance.

List of abbreviations

AEM	Anion exchange membrane
AEMWE	Anion exchange membrane water electrolysis
PEM	Proton exchange membrane
PEMWE	Proton exchange membrane water electrolysis
AEI	Anion exchange ionomer
PGM	Platinum group metal
HER	Hydrogen evolution reaction
OER	Oxygen evolution reaction
RDE	Rotating disk electrode
QA	Quaternary ammonium
SEM	Scanning electron microscopy
XRD	X-ray Diffraction
STEM	Scanning transmission electron microscopy
EDX	Energy dispersive X-ray spectroscopy
EIS	Electrochemical impedance spectroscopy
GDL	Gas diffusion layer
RHE	Reversible hydrogen electrode
SHE	standard hydrogen electrode
SCE	Saturated calomel electrode
fcc	Face centered cubic
I/C	Ionomer to catalyst weight ratio
R_{ct}	Charge transfer resistance
MEA	Membrane electrode assembly
RE	Reference electrode
E_a	Anode potential
E_c	Cathode potential
iR	Ohmic loss
ΔE	Cell voltage
η_a	Anode overpotential
η_c	Cathode overpotential

Introduction

Hydrogen is a clean energy transition pathway conveying renewable sources including solar, wind, and hydro, to the increasing energy demands around the globe [1,2]. The conversion of renewable energy to hydrogen is widely achieved by water electrolysis [3]. Proton exchange membrane water electrolysis (PEMWE) using an acidic Nafion® membrane has been reported to achieve outstanding activity and durability [4]. However, the PEMWE process relies on the use of platinum group metal (PGM) catalysts, platinum in particular for its cathodic hydrogen evolution reaction (HER) as well as iridium for its anodic oxygen evolution reaction (OER). The global scarcity of the two catalyst materials may significantly limit large scale PEMWE applications. Hence, besides many other research approaches in water electrolysis, substantial efforts are being made in researching anion exchange membrane water electrolysis (AEMWE) that allows for the use of non-PGM catalysts with its alkaline membrane electrolyte. An AEMWE performance that is similar to state-of-the-art PEMWE technology is thus being pursued, but with cheaper transition metal catalysts, membranes, ionomers, and construction materials [5,6].

Vincent et al. showed that optimizing the loading and ionomer content of electrodes for AEM electrolysis is crucial to reach optimum performance achieving 500 mA/cm^2 at 1.95 V using 1% K_2CO_3 electrolyte at 60 °C [7]. Pushkareva et al. studied AEM water electrolysis using nonprecious catalysts and found that the catalyst layer structure significantly affects the AEM electrolyzer performance [8]. Carbone et al. found that FAA3-50 alkaline membrane and ionomer with a $NiMn_2O_4$ anode catalyst showed excellent AEM performance at 80 °C achieving 530 mA/cm^2 at 2 V [9]. Park et al. electrodeposited Co_3S_4 nanosheets on Ni foam and applied it as a cathode to a single-cell AEM electrolyzer and achieved 431 mA/cm^2 at 2 V [10]. Zhiani et al. studied the AEM electrolyzer single cell by separating the anode and cathode polarizations. The results show that the modified electrode PdNiFeCo/C-Ceria on Ni foam showed the onset potential close to Pt/C modified Ni foam. The membrane electrode assembly (MEA) with PdNiFeCo/C-Ceria showed a cell voltage of 2.31 V compared to 2.22 V for Pt/C at the current density of 300 mA/cm^2 [11].

Ionomers, polymers with ionic groups attached to or as a part of the polymeric backbone, represent an important component in AEMWE cells with polymeric electrolyte membranes. Ionomers are used as binding agents for the catalysts to be uniformly distributed and stabilized at the electrode-electrolyte interface [12]. In principle, ionomers encompassing some ionic conductivity will extend the three-phase region, increasing the available active area within the catalytic layer during electrolysis of pure water. The ionomers in the catalytic layer facilitate the exchange of water and ionic products at the catalyst surface, via its charged functional groups [13]. However, due to the electrostatic/covalent interaction, the charged groups could occupy the catalyst sites [14] and compete with the half-cell reaction for the HER process, or incur oxidation products (generally for the OER process) [15], leading to additional potentials. Therefore, the electrode ionomer content is critical to cell performances. Ionomer content optimization depends on the type of ionomer, catalyst, and electrolyte, and has in general been conducted experimentally by a trial and error approach. The optimum content is then determined based on the lowest potential achieved for each electrode at a time, provided the other cell conditions are kept the same [7,16].

For a PEMWE operating cell, the HER potential is usually considered small because of the fast proton transfer kinetic from the electrolyte, through the Nafion® ionomer to the Pt catalyst surface [17]. Roca-Ayats et al. studied the effect of Nafion® content using an ex-situ rotating disk electrode (RDE) analysis [18]. The insignificant effect of Nafion® on the HER process was reported to be due to the negatively charged cathode surface electrostatically repels the Nafion®'s negatively charged functional group, SO^{3-} moiety [14,19]. In the single-cell electrolyzer scale, the optimized Nafion® content in PEMWE for the charge transfer between catalyst and electrolyte was found at 10–30 wt% of the total weight of catalyst and ionomer [17,20], whose performance also depends on the level of moisture, as reported by Modestino et al. [21] On the other hand, the OER potential is considered dominant in the PEMWE performance so that the cell voltage can be used for the determination of the corresponding anodic Nafion® content. The optimized performance, for a cell voltage of 1.57 V at

1 A/cm^2, was found with 11.6 wt% Nafion® of the total weight of the electrode that improved the anodic O_2 mass transfer and electronic contact resistances [22].

In AEM electrolysis, anion exchange ionomers (AEIs) with positively charged quaternary ammonium (QA) functional groups are used for the transport of OH^- ions at the catalyst surface [13,18]. However, the effect of AEIs on the electrode performances is more complicated than Nafion® in PEMWE. For the HER process, the positively charged QA moiety induces specific adsorption and electrostatic effects which results in the H_2O HER reactants in the IHP experiencing a lower effective potential in the presence of AEI than in the presence of Nafion and inhibit the electrocatalyst activity, as reported by Bates et al. [14] Moreover, as further reported by Bates et al., the ammonium functionalities of QA have been shown to affect the formation of HER intermediates at Pt surfaces and NiMo [14]. For the anodic OER process, the electrode performance, as reported by Li et al. [15], is influenced by oxidation of phenyl groups in the AEI backbone. The phenyl groups were generally introduced for hindering hydroxide degradation. However, under applied OER potentials, the electrochemical oxidation of phenyl groups can neutralize QAs and reduce the local pH, which in turn may cause a reduction in the catalytic activity [15]. All these factors complicate the effect of AEI on the corresponding electrode and thus the AEI content needs to be determined for an optimized electrode performance.

Given the very different AEI inhibition mechanisms for AEMWE anode and cathode, optimization of the two electrodes has to be performed separately. This is best done in an operating cell rather than being based on ex-situ techniques such as rotating disc electrodes since the performance in the latter device is not always well correlated with that in the former [23]. However, for the AEI optimization inside an operating AEMWE, a major challenge is to distinguish the performance of the anode from that of the cathodic. One solution is in-situ half-cell measurements that specifically measure each half-cell potential with minimal interference with the electrolysis process.
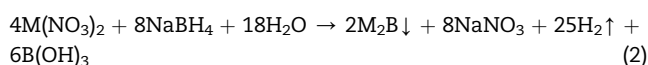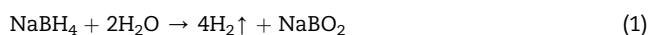
Therefore, this study, for the first time to the best of our knowledge, uses in-situ half-cell analysis in an AEMWE with reference electrodes to differentiate between the performance of a NiO anode and that of a Ni/C cathode at various AEI content during the cell operation. With this novel approach, the AEI-Ni catalyst composition was specifically optimized for each half-cell process (HER/OER). The in-situ results were consistent with the results of the RDE analysis. PGM electrodes (Pt/C cathode and Ir anode) were also tested, and their performance was compared with the optimized Ni-based electrodes. The post-mortem electrode surface morphologies with different AEI content were investigated using scanning electron microscopy (SEM) analysis, and the corresponding AEI distributions were analyzed by elemental mapping using energy dispersive X-ray (EDX) techniques. The results show that the cathode is more sensitive to the actual amount of AEI content than the anode and the optimized AEI content for a Ni-base cathode is 10 wt% of the coated catalyst. The precise identification of the optimum content of ionomer for every relevant combination of catalyst, catalyst layer, electrolyte, and concentrations of KOH in the feedwater is a significant challenge in AEM water electrolysis. We do believe, however,

that the current approach will significantly improve the efficiency of such investigations.

Experimental

Catalyst synthesis

Nickel nitrate hexahydrate $Ni(NO_3)_2.6H_2O$ (≥97.0%, Sigma Aldrich) were dissolved in 500 mL water (18.2 MΩ cm, 3 ppb TOC, Milli-Q® Integral ultrapure water). Sodium borohydride ($NaBH_4$, 98%, Sigma Aldrich) solution was added dropwise. Upon $NaBH_4$ addition, bubbles were observed, and a black precipitate formed simultaneously. The molar ratio between sodium borohydride and nickel precursor was kept at three. The chemical reactions for catalyst formation using $NaBH_4$ can be described as follows [24].

$$NaBH_4 + 2H_2O \rightarrow 4H_2\uparrow + NaBO_2 \qquad (1)$$

$$4M(NO_3)_2 + 8NaBH_4 + 18H_2O \rightarrow 2M_2B\downarrow + 8NaNO_3 + 25H_2\uparrow + 6B(OH)_3 \qquad (2)$$

The solution was stirred for 1 h to ensure complete reduction. For Ni/C, carbon support (Ketjen black ec600j-d(AkzoNobel, Netherlands)) was added to make 60% Ni/Ketjen black, and the solution stirred for another hour. The precipitate was centrifuged 5 times at 8000 rpm for 6 min and cleaned with water and ethanol three times. The produced precipitate was then dried at 80 °C overnight in a vacuum oven. Ni/C was annealed in a 5%H_2/Ar atmosphere while NiO was annealed in an air atmosphere at 500 °C for 6 h.

Structural and electrochemical characterization

The morphology of produced catalysts was studied using Hitachi S-5500 FESEM (Krefeld, Germany). The structural and crystalline characteristics were investigated by X-ray diffraction (XRD) with a Bruker D8 A25 DaVinci device with CuKα radiation. The average wavelength of the radiation was 1.5425 Å. Ex-situ Raman spectroscopy was carried out using WITec alpha300 R Confocal Raman device with 533 nm (50 mW). All spectrum peaks were calibrated against the value of 520.7 cm^{-1} of a silicon wafer.

Rotating disk electrode measurements

The electrochemical analysis was done in a three-electrode cell using a rotating disk electrode (PINE Research) and an (Ivium-n-Stat) multi-channel potentiostat. A graphite rod (PINE Research) served as the counter-electrode. A Hg/HgO electrode (Pine Research) was used as the reference electrode. The working electrode was fabricated by depositing catalyst ink on glassy carbon (GC) electrodes (5 mm diameter, Pine Research). The GC electrode was polished using aqueous alumina Al_2O_3 suspension (5 and 0.25 μm, Allied High-Tech Products, Inc.) on felt polishing pads. The GC electrode was washed, sonicated in ethanol and water for 5 min, and finally rinsed with water. The catalyst ink was prepared by dispersing 10 mg of catalyst (Ni, Ni/C, Pt/C (60%, Alfa Aesar), Ir

black (Alfa Aesar)) in 1.0 mL of a solution [500 μL water, 500 μL isopropanol, and ionomer solution]. The ionomer used was either Nafion (5 wt%, Alfa Aesar) or anion exchange ionomer Fumion FAA-3 (10 wt%, Fumatech, full cell store). The Fumion FAA-3 ionomer to catalyst ratio (0.2, 0.5, 0.8, and 1) was varied in ink composition. The ink was sonicated for 30 min in an ice bath. Catalyst loading on the GC surface was kept 250 μg/cm^2.

All the electrochemical measurements were conducted in N$_2$-saturated alkaline 1 M KOH electrolyte at room temperature (20 ± 2 °C). The electrolyte was purged for 30 min with N$_2$ gas before using and during the experiment to remove any dissolved gases during electrochemical measurements. The electrolyte was prepared by using KOH (Sigma Aldrich), and water (18.2 MΩ cm, Milli-Q® Integral ultrapure water). The electrolyte was purified according to the procedure reported by L. Trotochaud et al. [25].

For the HER: Before the measurement, the working electrode underwent electrochemical activation by cycling between −0.8 and −1.5 V at a scan rate of 100 mV s^{-1} for 50 cycles until reproducible cyclic voltammograms (CVs) were obtained. Polarization curves were recorded by linear sweep voltammetry (LSV) in a potential range of −0.8 to −1.5 V vs. Hg/HgO at a sweep rate of 1 mV s^{-1} continuously rotating the electrode at 1600 rpm. Electrochemical impedance spectroscopy (EIS) was carried out for further investigation of the electrode kinetics and electrode-electrolyte interface. The EIS measurements were performed potentiostatically at specific overpotentials (−250 mV) in a frequency range of 0.1— 10^5 Hz with a perturbation amplitude of 10 mV. In this work, ohmic losses (iR) drop was compensated at 85% of high-frequency resistance, which was measured by the EIS technique at −1.3 V versus Hg/HgO. The potential was compensated by the following equation:

$$E_{compensated} = E_{measured} - iR \quad (V) \qquad (3)$$

where $E_{compensated}$ and $E_{measured}$ denote as the compensated and measured potentials, respectively.

For the OER: Before the measurement, the working electrode underwent electrochemical activation by cycling between 0.2 V and 0.9 V vs. Hg/HgO at a scan rate of 100 mV s^{-1} for 50 cycles. The linear sweep voltammetry (LSV) polarization curves were recorded in a potential range of 0.3—0.9 V vs. Hg/HgO at a sweep rate of 1 mV s^{-1} under continuous stirring at 1600 rpm. In this work, after recording polarization curves, the iR drop was compensated at 85%, which was measured by the EIS technique at 0.8 V versus Hg/HgO. The electrochemical impedance spectroscopy test was collected in a frequency range of 0.1— 10^5 Hz with an amplitude of 10 mV alternative current (AC) perturbation at 0.8 V vs Hg/HgO.

The Hg/HgO reference electrode potential was calibrated versus reversible hydrogen electrode (RHE) potential and the following equation was used:

$$E_{vs RHE} = E_{vs Hg/HgO} + 0.9 \qquad (4)$$

Gas diffusion layer (GDL) preparation

Catalyst inks for catalyst (Ni, Ni/C, Pt/C (60%, Alfa Aesar), Ir black (Alfa Aesar) were fabricated by mixing catalyst powder with water, isopropanol (1:1), and anion exchange ionomer Fumion FAA-3 (10 wt%, fuel cell store). The ionomer

weight percent (wt%) was either 10, 20, 30, or 40. The solution was sonicated for 30 min in an ice bath. The catalyst loading was kept equal to 5 mg/cm^2 for all catalysts. Cathode and anode catalyst layers were sprayed at 60 °C on Toray 090 carbon paper (fuel cell store) as catalyst coated substrates. The membrane Fumapem-3-PE-30 (Fumatech, Germany) was sandwiched between cathode and anode gas diffusion electrodes. The membrane electrode assemblies (MEAs) were conditioned and exchanged to the OH form in 1 M KOH before used.

In-situ reference measurements

The in-situ activities of the catalyst-coated substrate samples were analyzed by measuring their corresponding half-cell potential during an AEMWE operation, as shown in Fig. 1. In this AEMWE structure, the cell was operated and analyzed with electrolyte flowing at each side. As shown in Fig. 1, a reference electrode capillary was inserted from the anode side, through the GDL, touching the AEM surface. This created an ionic pathway between the anode electrode and a Hg/HgO reference electrode. In this way, the OER half-cell potential can be specifically analyzed. A similar design was applied at the cathode side to analyze the HER potential. The assembled AEMWE cell was tested and analyzed under ambient temperature, as shown in Fig. 2. During the test process, 1 mol dm^{-3} KOH solution was circulated at each side of the AEMWE respectively, at 50 cm^{-3} min^{-1}. The power input was generated by a HewlettPackard® E3610A DC power supply, and the cell performance was measured at 5 different potential increments, from 1.5 V to 2.0 V. The corresponding current was recorded 5 min after each potential increment. Besides, each half-cell electrode potential (OER or HER) was measured versus a Hg/HgO reference electrode at the upper port of the capillary, as shown in Fig. 2. Note that homemade Hg/HgO reference electrodes whose fabrication process was summarized in supplementary information and Figs. S1 and S2 were used for the in-situ half cell measurement.

The corresponding reference electrode (RE) potential calibration used for HER measurement (RE$_{HER}$) was −156.8 mV ± 0.1 mV vs.SCE or 83.8 mV ± 0.1 mV vs. SHE ; for OER measurement (RE$_{OER}$) was −157.2 mV ± 0.1 mV vs. SCE or 84.2 mV ± 0.1 mV vs. SHE, of which stability was analyzed and included in the supplementary information. For each type of catalyst coated substrate sample, the in-situ activity analysis was repeated 3 times. The external resistance including the current meter has a 1 Ω resistance which was not excluded from the data. The cell assembly and engineering design of the cell are shown in Figs. S3 and S4.

During the in-situ measurements process, three potential values can be measured, as shown in Fig. 2, at each current level, the cell voltage (ΔE) recorded by the DC power supply, the anodic potential E_a measured between the anode and RE$_{OER}$, the cathodic potential E_c measured between the cathode and RE$_{HER}$. The half cell measurements were validated when the difference between E_a and E_c matches with the ΔE, at an open circuit potential, as shown in the following equation:
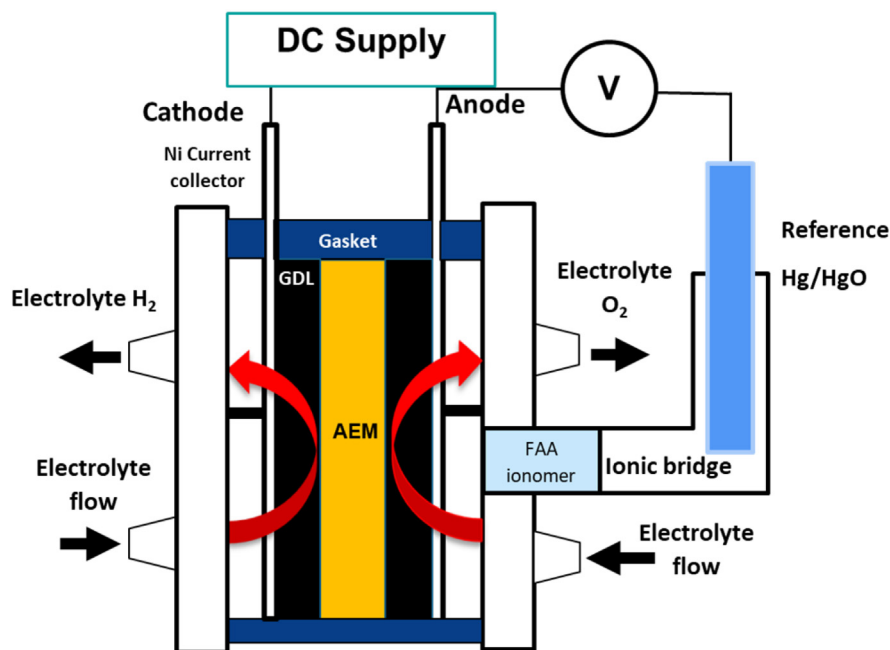
Fig. 1 — A schematic diagram describing the in-situ half-cell measurement within an operating AEMWE. Note that, in this diagram, only anode measurement is presented; in practice, both electrodes were analyzed using the same strategy.

$$\Delta E \; at \; OCP = \; E_a - E_c + (RE_{OER} - RE_{HER}) \qquad (5)$$

Post-mortem analysis

SEM analysis was conducted on the surface of Ni catalyst coated substrate samples. To ensure a sufficient conductivity, each substrate sample was stabilized on an aluminum stub, using carbon tapes. The SEM analysis was conducted with a Hitachi® SU-5000 SEM, and images were taken at X90 magnification, using back-scattering electron (BSE) mode. The elemental analysis was taken at ×5k magnification, using energy dispersive X-ray spectroscopy (EDX) mapping.

Stability analysis of the AEMWE cell

Before the in-situ half-cell analysis, Ni/C and NiO GDEs were assembled within the AEMWE structure for a stability test with 1000 cycles of CV at a 10 mV s^{-1} scan rate. The result (Fig. S5) shows an insignificant change in the cyclic voltammogram curves before and after 1000 cycles.

Results and discussion

Catalyst characterization

Before the in-situ half cell measurement with reference electrodes, the structure and the electrochemical properties of the synthesized Ni catalysts were examined using SEM, STEM, XRD, and RDE analyses.

Fig. 3 shows SEM and STEM images of produced nickel catalyst morphology. SEM in Fig. 3.a and STEM in Fig. 3.c show images of the Ni/C catalysts while Fig. 3.b (SEM) and 3.d (STEM)

show the NiO catalysts. As shown in Fig. 3.a, an interconnected network of Ni/C can be seen, which is formed by the fused particles shown in Fig. 3.c. Such a Nanosheet morphology is commonly attained using the chemical reduction synthesis process [26—32]. Besides, the produced NiO can be seen as flakes (Fig. 3.b) which was formed by stacking and agglomeration of a nanosheet morphology as shown in Fig. 3.d.

The structure of the synthesized Ni catalysts was further studied using XRD (Fig. 4.a) and Raman spectroscopy (Fig. 4.b). Fig. 4.a shows X-ray diffraction (XRD) patterns of synthesized Ni (blue) and NiO (grey) after the annealing process. For Ni catalyst, the XRD pattern shows two diffraction peaks at $2\theta = 44.5°$ and $51.9°$, corresponding to the (111) and (200) crystal planes of the nickel metal face-centered cubic (fcc) structure based on the JCPDS card 04—0850 [33]. The NiO pattern shows three distinct peaks at $2\theta = 37.2°$, $43.2°$, and $62.8°$ which correspond to the (111), (200), and (220) diffraction planes of the face-centered cubic (fcc) NiO structure (JCPDS card 47—1049) [34]. The high peak intensity indicates the high crystallinity of the NiO nanosheet structure. Overall, only one crystal structure was detected in each diffractogram, indicating a high purity for both synthesized catalysts.

Fig. 4.b shows the Raman spectrum of Ni/C and NiO catalysts. For the Ni/C spectrum, the peaks D and G are ascribed to the carbon support [35—37], no peak was found corresponding to the Ni because Ni is a face-centered cubic (fcc) metal and does not show any polarizability change during vibration in the Raman spectrum [38]. A change in polarizability during molecular vibration is a necessary condition for obtaining the Raman spectra of a sample [38]. The NiO Raman spectrum shows peaks at wavenumbers 400, 530, 730, 900, 1090 cm^{-1}. The Raman peaks at 400 and 530 cm^{-1}
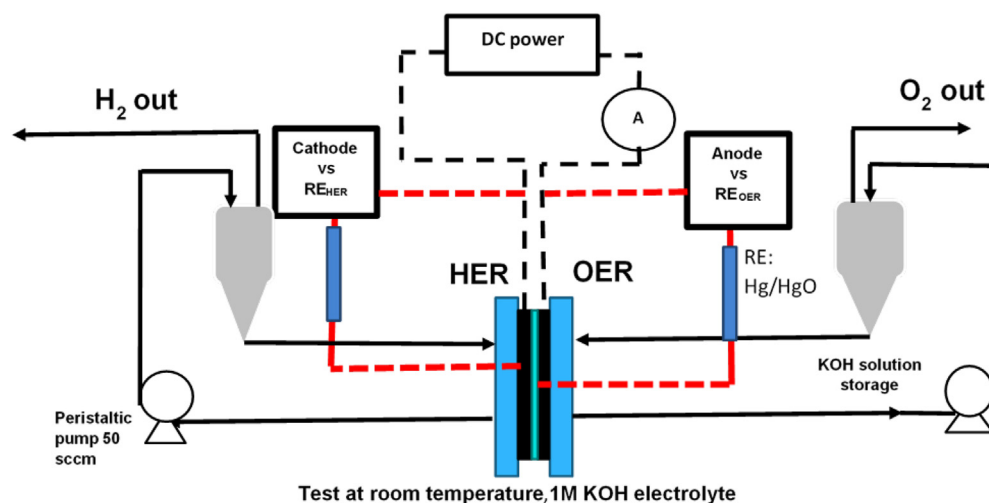
Fig. 2 – A process diagram describing the in-situ half-cell measurement on the HER and OER of an operating AEMWE.

correspond to the one-phonon (1P) transverse optical (TO) and (1P) longitudinal optical (LO) vibrational modes of NiO, respectively. The peaks at 730, 900, 1090 cm^{-1} correspond to the two-phonon (2P)$_{TO}$ 2P $_{(TO+LO)}$, and 2P$_{LO}$ of NiO vibrational modes, respectively [39,40]. The existence of LO mode can be attributed to structural defects and surface imperfections [39,40].

Electrochemical characterization

RDE measurements

A preliminary study on the catalyst-ionomer effect was conducted by testing catalyst activity with various anion exchange ionomer/catalyst (I/C) weight ratios with RDE analysis. The resulting LSV curves are summarized and compared in
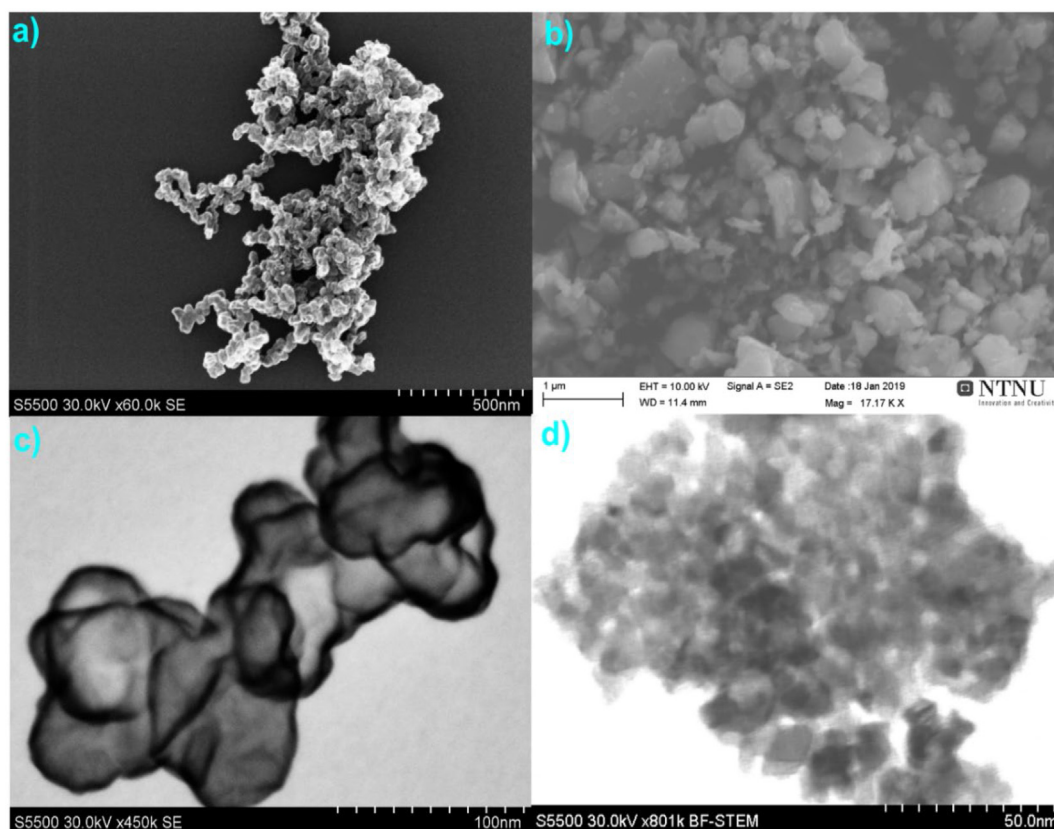

Fig. 3 – a), c) SEM and STEM images of Ni/C, b) and d) SEM and STEM images showing the morphology of the synthesized NiO.
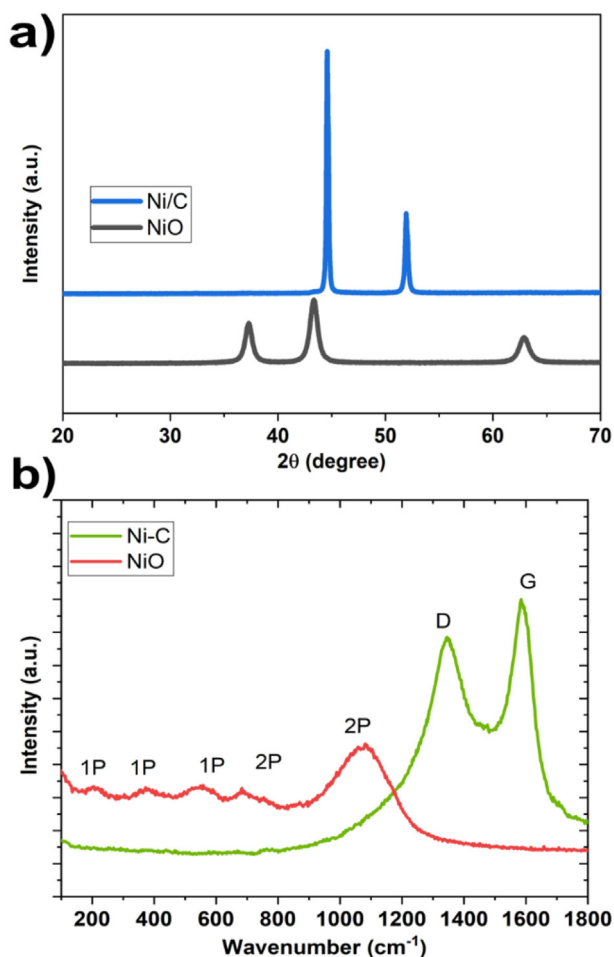
Fig. 4 — a) X-ray diffraction patterns b) Raman spectra of the synthesized nickel catalysts.

Fig. 5.a for Ni/C and Fig. 5.b for NiO. Fig. 5.a shows the LSV curves of Ni/C catalysts with 0.2–1 (I/C) ratios of Fumion AEI contents. A significant difference can be seen with 0.1 V difference between the lowest (I/C = 0.2) and the highest (I/C = 1) potentials at −10 mA/cm² current density. The I/C = 0.5 curve

is very similar to the I/C = 0.2 curve, indicating the optimum ionomer loading for the Ni/C HER activity could be between 0.2 and 0.5 (I/C) ratio which is comparable to results obtained by Alia et al. [16].

On the other hand, the NiO curves were not strongly dependent on the amount of anion exchange ionomer, as shown in Fig. 5.b. The curves resulting from different (I/C) ratios are closely aligned, with 0.025 V maximum potential difference at 10 mA/cm² current density, which suggests that the effect of ionomer content is small on the anodic OER process.

Fig. S6.a shows current versus potential recorded during linear sweep voltammetry (LSV) for Ni/C with different ionomers. Fig. S6.b shows the results of electrochemical impedance spectroscopy, presented as impedance-plane plots, for Ni/C with different ionomers. For Ni/C with the Fumion ionomer, the current is −10 mA/cm² at −0.36 V in 1 M KOH, as compared to −0.33 V vs. RHE required to achieve the same current density for the catalyst with the Nafion ionomer in 1 M KOH. The electrochemical impedance spectroscopy data for a Ni/C catalyst are shown in an impedance plane plot in Fig. S6.b. The impedance complex plane plot can be fitted to an R(QR) circuit which gives a depressed semicircle (Fig. S6.b) [41]. The charge transfer resistance (R_{ct}) was obtained after fitting the data to an R(QR) circuit and determining the difference between the high frequency and low-frequency converging intercepts of the real axis.

The catalyst with the Fumion AEI has a charge transfer resistance (R_{ct} = 36 Ω) approximately twice of that of the catalyst with the Nafion ionomer (18 Ω). Both the LSV and the impedance data show unequivocally that both catalysts are substantially more active for the HER with the Nafion ionomer than with Fumion. Fumion AEI resulting in a lower HER activity as compared to Nafion is consistent with previous results obtained for NiCo and NiFe catalysts [42].

The electrode activity difference incurred by the use of Fumion and Nafion is likely to be related to the adsorption of the cation functional groups in the Fumion anion exchange ionomer (quaternary ammonium, QA), which are absent in Nafion [14,19]. Specific adsorption of the QA⁺ moiety and the electrostatic effects of AEI on Ni/C would result in the HER
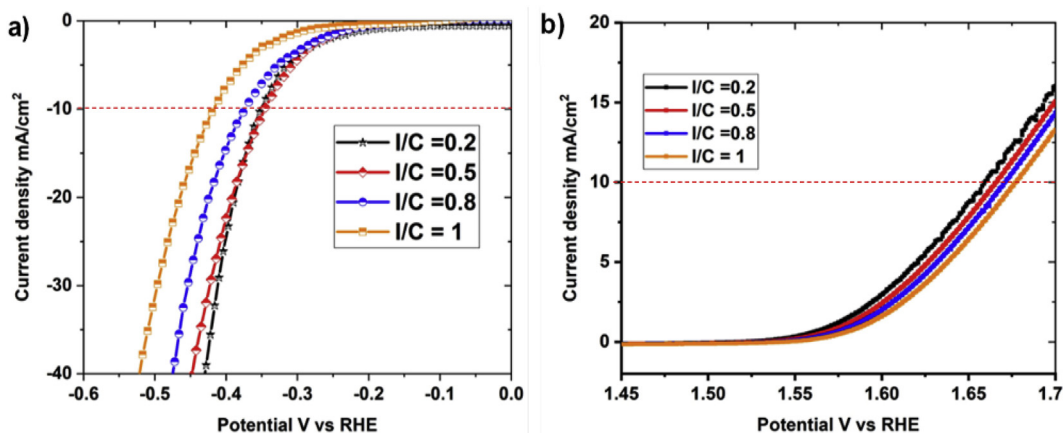

Fig. 5 — LSV of the synthesized a) Ni/C. b) NiO catalysts with different ionomer to catalyst (I/C) ratios obtained in 1 M KOH at a sweep rate of 1 mV s⁻¹ and ambient conditions.

reactants in the inner Helmholtz plane (IHP) experiencing a lower magnitude of the effective potential at the IHP in the presence of AEI than in the presence of Nafion [14]. The adsorption interactions include (i) cation-hydroxide-water co-adsorption and (ii) phenyl group adsorption [43]. The adsorption impacts the HER LSV curves by blocking the active sites of the catalyst [43].

Fig. S6.c and S6.d show LSVs in the OER region for the NiO catalyst using Nafion and Fumion ionomers, respectively, and the corresponding impedance complex plane plots. The Fumion AEI resulted in lower OER activity compared to Nafion ionomer. The high-frequency resistance of NiO using Nafion or Fumion was almost the same $(3.2 \pm 0.1 \ \Omega)$ for all experiments in 1 M KOH and was subtracted from the impedance plot. R_{ct} values using Nafion ionomer $(6.1 \ \Omega)$ was lower compared to Fumion $(8.6 \ \Omega)$. The detrimental effect of AEI Fumion on OER is reported to depend on phenyl adsorption of the ionomer backbone and the oxidation products under the applied anodic potentials [15,44]. Pt group metal (PGM) catalyst shows better performance than Ni-based catalysts using Nafion or Fumion AEI as in Fig. S7.

The RDE results show that for the Ni catalysts, the ionomer content has more impact on the cathodic HER than on the anodic OER performance.

In-situ half cell reference analysis
Ionomer-catalyst interaction at the cathode. The cell voltage between the anode and cathode was controlled and recorded by a DC power supply. As usual, we will refer below to the electrode potential (or half-cell potential) as the measured potential of a given electrode with respect to the reference electrode, and cell voltage as the potential difference between the anode and the cathode. Each half-cell measurement (anode/cathode) was recorded with respect to a calibrated Hg/HgO electrode, and the values have been converted vs. standard hydrogen electrode (SHE). The in-situ single cell test rig fixed with a reference electrode capillary allows for three simultaneous measurements on anode potential (E_a), cathode potential (E_c), and cell voltage. The following results include the cell voltages and half-cell potentials measured with anodes or cathodes containing varying Fumion AEI contents while keeping the opposite electrode fixed.

The AEMWE cells were operated with different amounts of Fumion AEI (10–40 wt%) in the Ni/C cathode catalytic layers.
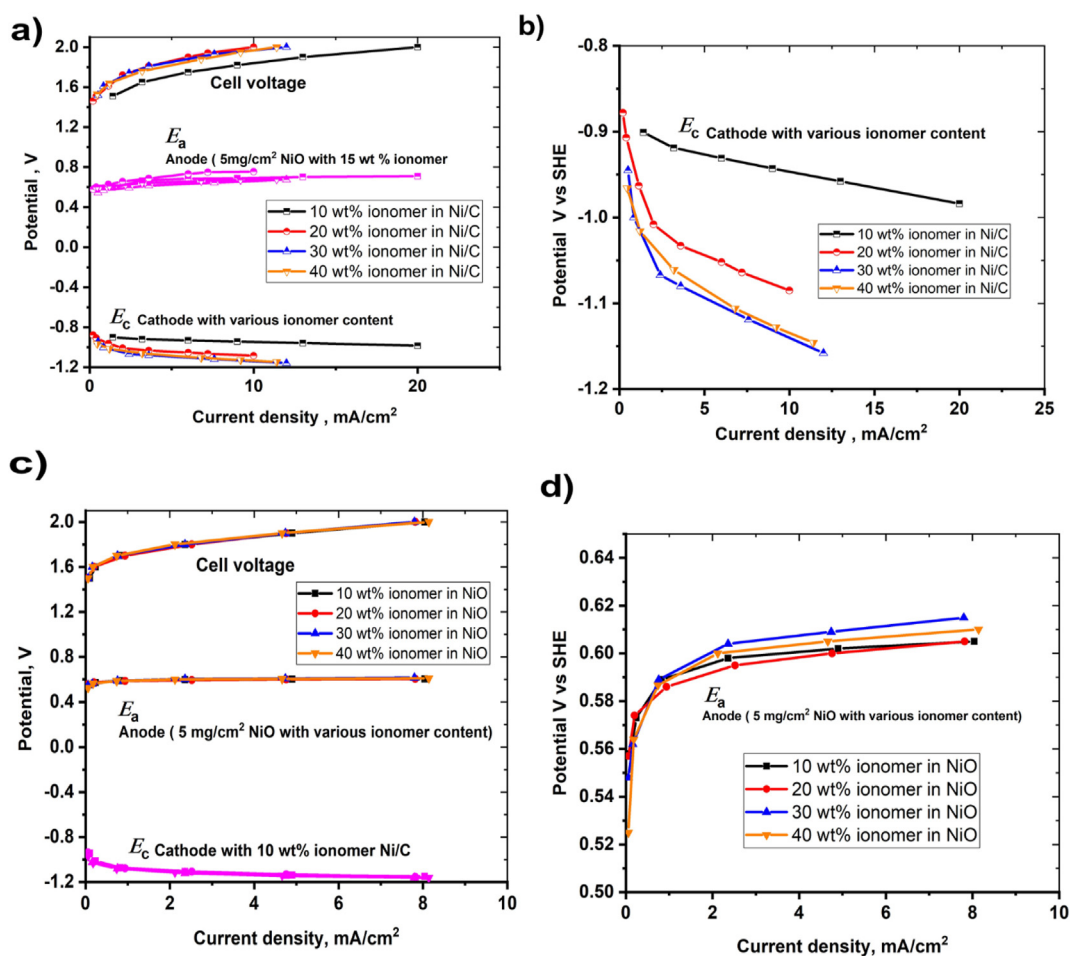

Fig. 6 – Plotted diagrams of a), c)cell voltage, anode potential (E_a), and cathode potential (E_c) vs current density for NiO and Ni/C systems, b) and d)electrode potential vs current density measured from the test AEMWE with different ionomer contents at the Ni/C cathodes and NiO anodes respectively.
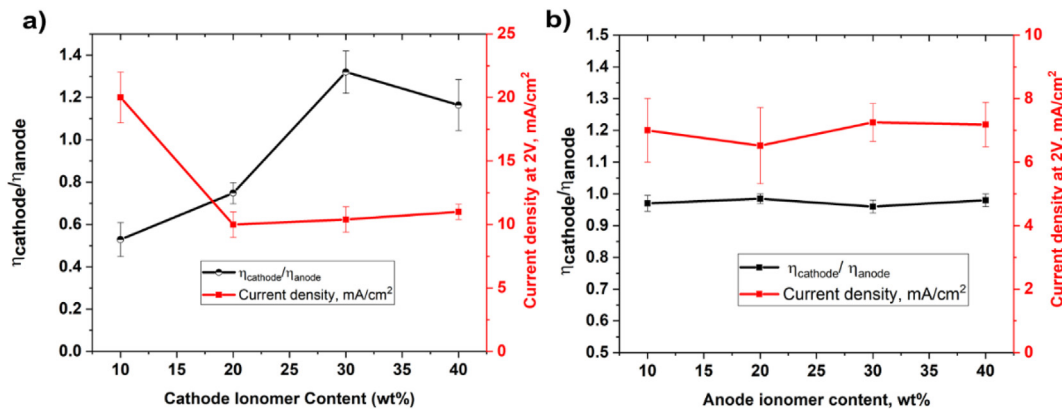
Fig. 7 — a) $\eta_{cathode}/\eta_{anode}$ **and current density at a cell voltage of 2 V vs cathode ionomer content, b)** $\eta_{cathode}/\eta_{anode}$ **and current density at a cell voltage of 2 V vs anode ionomer content.**

In these measurements, the amount of Fumion AEI in the anode NiO catalytic layers was 15 wt%. The measured cell voltage is plotted in Fig. 6.a. The corresponding cathodic potentials, E_c, are plotted separately in Fig. 6.b.

As shown in Fig. 6.a, the electrode potentials for the NiO anode, which all contained 15% ionomer, were identical within 2% whatever of the amount of AEI in the Ni/C cathode. The results indicate that the anodes were extensively analyzed, validating the reliability of the in-situ half-cell measurement setup. On the other hand, the total cell voltage and cathode potential were highly affected by changing the cathode AEI content. In particular, the cell with 10 wt% AEI content cathode achieved a much higher current density than others at the cell voltage of 2 V, as shown in Fig. 6.b. The measurements were repeated for the MEA of ionomer content (20 wt%) and the results are shown in Fig. S8, demonstrating good test reproducibility.

The 10 wt% ionomer Ni/C cathode gave the lowest potential contribution of all the tested Ni/C cathodes (Fig. 6.a and 6.b). The potential contribution increases with increasing AEI content (from 10% to 30%), with a 0.2 V difference at 10 mA/cm^2, which is a larger change than observed from the RDE measurements (Fig. 5.a).

Ionomer-catalyst interaction at the anode. AEMWE cells with a Fumion AEI content in the range 10 through 40 wt% in the NiO anodes and 10 wt% in the Ni/C cathode ionomer content were tested. The corresponding cell voltage is given in Fig. 6.c for the different anode compositions along with the anode and cathode electrode potentials. The measured cell voltage, anode potential E_a, and the cathode potential E_c were all independent of the amount of AEI in the NiO anodes. As shown in Fig. 6.d, the resulting electrode potentials for the anode did not differ significantly at any current, and the maximum difference between the half-cell potential is as small as 0.02 V at a current density of 8 mA/cm^2, which is consistent with the RDE measurements in Fig. 5.b. These results suggest that the effect of AEI content is insignificant for NiO anodes and doesn't change the electrode activity drastically.

These results suggest that the impact on AEI content is significant in the Ni/C cathode performance while NiO anode

catalytic layer electroactivity is independent of ionomer content. One possible reason is that the ionomer content may influence the surface morphology of the coated layers and thus the electrode activity. This hypothesis was verified by examining the surface of the Ni/C cathode and NiO anode samples using SEM imaging.

From the in-situ reference measurements and the separation of the cathode and anode electrode potentials, the ohmic losses iR can be obtained using the following equation:

$$\Delta E = 1.23 + \eta_{anode} + \eta_{cathode} + iR \tag{6}$$

in which ΔE is the cell voltage, 1.23 is the reversible cell voltage, η_{anode} is the anode overpotential, $\eta_{cathode}$ is the cathode overpotential, and iR is the ohmic losses.

Using equation (6) a clear separation of the effect of ionomer content on electrode potential and ohmic losses can be obtained. Fig. 7.a displays the percentage of the cathode to anode overpotential and current versus cathode ionomer content. The cathode with an ionomer content of 10 wt% gives the lowest cathode overpotential, the smallest ratio $\eta_{cathode}/\eta_{anode} = 0.5$, and the largest produced current of 20 mA/cm^2 at a cell voltage of 2 V. As the ionomer content increases, the cathode overpotential increases and the ratio $\eta_{cathode}/\eta_{anode}$ increases up to 1.3, and the cell current density decreases to around 10 mA/cm^2 at a cell voltage of 2 V. The data in Fig. 7.a is extracted from Fig. S9. Fig. S9 shows the detailed overpotential contribution cathode, anode, and ohmic losses of MEAs with cathode electrodes with ionomer contents of 10, 20, 30, and 40 wt%. The associated ohmic losses are of 0.28 ± 0.02, 0.16 ± 0.02, 0.18 ± 0.01, and 0.2 ± 0.02 V, respectively, at a cell voltage of 2 V for MEAs with cathode ionomer content of 10, 20, 30, and 40 wt%. The high ohmic losses may be due to the high ohmic resistance of the external resistances including current meter used (1 Ω), in addition to the normal reasons for ohmic losses of cell design, electrolyte conductivity, and membrane. In general, the ohmic loss (iR) is the difference between the black solid curve and the dashed horizontal line, the anode overpotential as the red minus the black solid, and the cathode overpotential is as the blue minus the red. Fig. S9.e shows clearly the effect of cathode ionomer content on
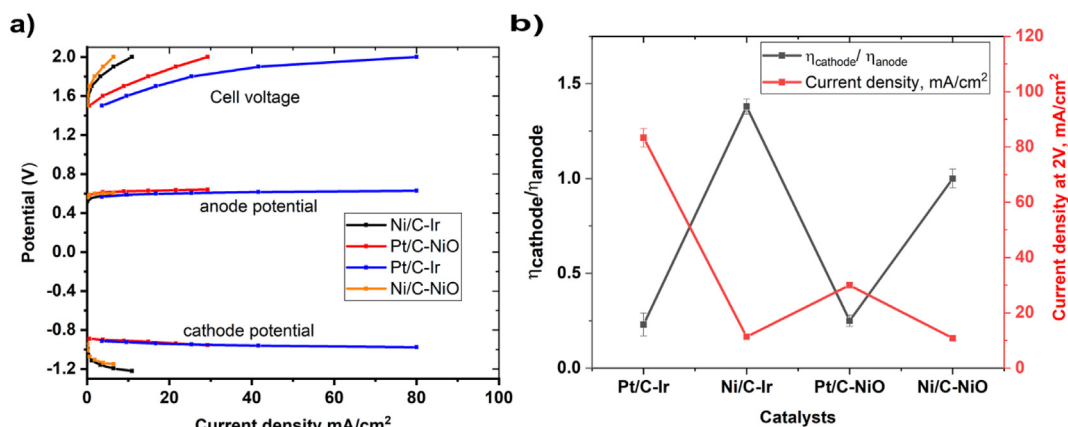
Fig. 8 — a) Cell voltage, anode, and cathode potential contribution at the same ionomer content of Pt/C—Ir, Pt/C—NiO, Ni/C—Ir, and Ni/C—NiO and b) the percentage between cathode to anode overpotential and current density at 2 V for various catalysts.

electrode potentials vs RHE and the corresponding current density.

Fig. 7.b shows the percentage between cathode to anode overpotential and current density at a cell voltage of 2 V versus ionomer content (wt%) in the anode electrode. The figure shows that anode overpotential and the resulting current density are independent of ionomer content. The ratio between anode and cathode overpotentials equals approximately one and is independent of ionomer content. The data in Fig. 7.b is extracted from Fig. S10. Fig. S10 shows detailed polarization curve with the cathode and anode overpotentials, and ohmic losses of MEAs with anode ionomer contents of 10, 20, 30, and 40 wt%. The cells with anode ionomer contents of

Table 1 — Anode and cathode potential to achieve the standard 10 mA/cm^2.

Cathode	Anode	Anode potential vs SHE to achieve 10 mA/cm^2	Cathode potential vs SHE to achieve −10 mA/cm^2
Pt/C	Ir	0.585	−0.925
	NiO	0.620	
Pt/C	Ir	0.585	−0.925
Ni/C			−1.220

10, 20, 30, and 40 wt% possess ohmic losses of 0.235 ± 0.01 V for all ionomer contents at a cell voltage of 2 V. Fig. S10.e shows
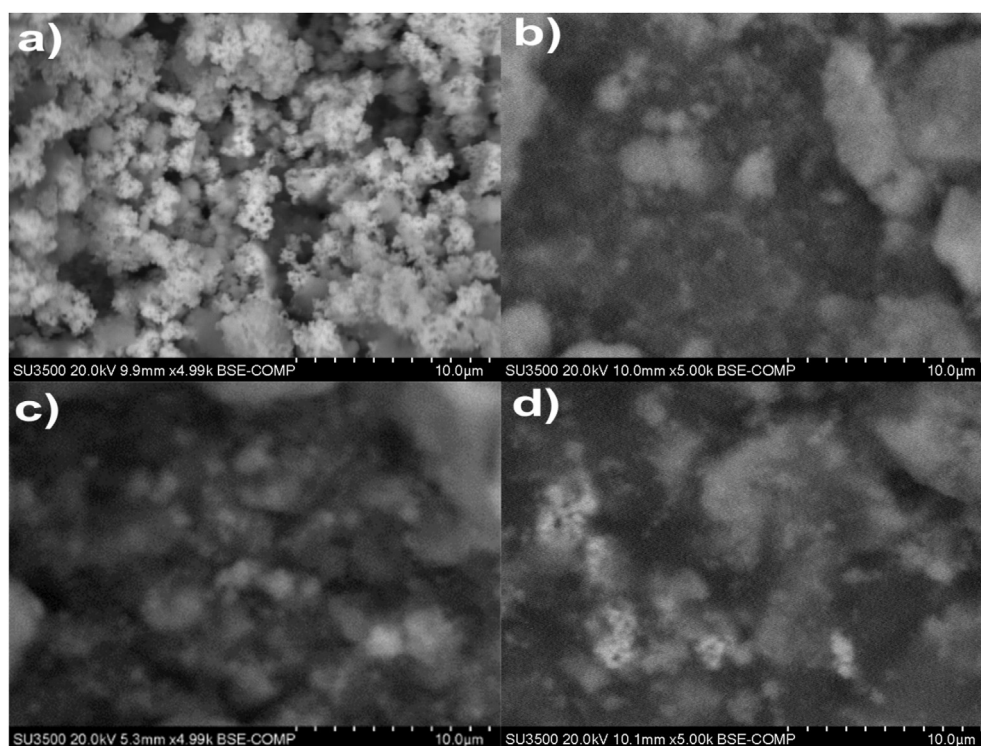

Fig. 9 — SEM images of Ni/C cathode catalytic layers with ionomer content of a)10 wt%, b)20 wt%, c)30 wt%, and d)40 wt%.
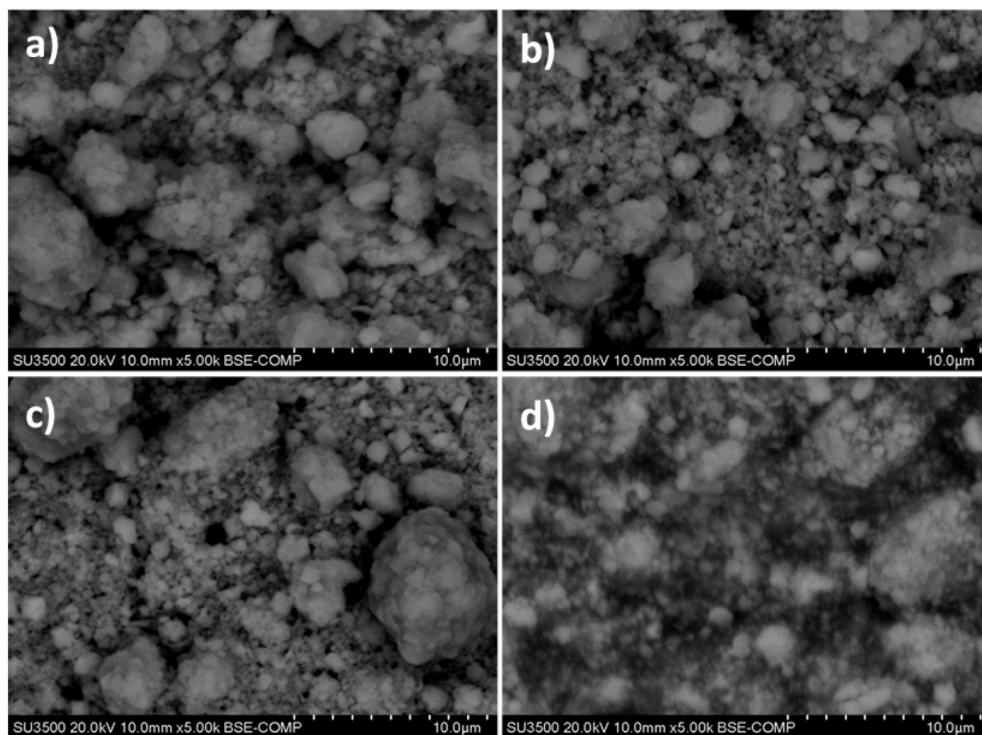
Fig. 10 – SEM images of NiO anode catalytic layers with ionomer content of a)10 wt%, b)20 wt%, c)30 wt%, and d)40 wt%.

clearly the effect of ionomer content on anode electrode potentials vs RHE and the corresponding current density.

Comparison between PGM and non-PGM-AEI electrodes. To separate the effect of anode and cathode activity (PGM vs non-PGM), we carried out experiments for the cell combinations Ni/C cathode-Ir anode and Pt/C cathode-NiO anode. Fig. 8.a shows the cell voltage and the corresponding electrode potentials for four different combinations of cells, viz. a cell with a Ni/C cathode-NiO anode, Ni/C cathode-Ir anode, Pt/C cathode- NiO anode, and Pt/C cathode-Ir anode with the same ionomer content in the cathode and the anode. Fig. 8.b shows the percentage between cathode to anode overpotential and current density at a cell voltage of 2 V for different catalyst combinations. Fig. 8.b shows that Pt/C–Ir cell shows the lowest percentage of the cathode to anode overpotential and the highest current density at a cell voltage of 2 V. Fig. S11 shows the detailed cell overpotential contributions of the anode, cathode, and ohmic losses for these cell combinations. With the same HER Pt/C catalyst and AEI content of 15 wt% in the catalytic layer, a current density of 10 mA/cm^2 was achieved at 0.585 V vs SHE with an iridium anode as compared to an anode with NiO catalysts at which this current density was reached at 0.620 V vs SHE, i.e. a difference of merely 35 mV. The best catalytic activity is obtained with Pt/C–Ir system using anion ionomer while the lowest activity is Ni/C–NiO. The cathode, on the other hand, affects the performance much more significantly. With an identical anode, viz. an Ir catalyst with an ionomer content of 15 wt%, a Pt/C cathode (20 wt% ionomer) gave a much higher activity than a Ni/C cathode (20 wt% ionomer); for the Pt/C

cathode, the potential is −0.925 V at −10 mA/cm^2 vs SHE compared to −1.220 V vs SHE for Ni/C at the same current density, c. f. Table 1.

These results highlight the importance of the cathode since the additional overpotential associated with replacing platinum at the cathode with a non-PGM catalyst is much higher than those associated with the corresponding replacement at the anode. While several reports have been published showing the decreased activity for Pt catalysts at high pH [45,46], our results show that the cathode may actually be the electrode causing the larger losses by far. This is important since it demonstrates a potential for huge cost savings at an insignificant performance penalty, simply by replacing the iridium-based catalysts at the anode. We emphasized the fact that these results were obtained from a working electrolysis cell.

Post-mortem SEM analysis on electrode morphology. The surfaces of the Ni/C cathodes with different AEI contents were examined with an SEM using backscattering electron (BSE) mode that contrasts elemental differences, i.e. showing the heavier Ni material as bright regions and the lighter carbon substrate as dark regions. SEM images of the various Ni/C cathode catalyst samples are given in Fig. 9, and, show the changes in surface morphology for the different AEI contents. The Ni distribution (bright regions) with 10 wt% ionomer (Fig. 9.a) is homogenous and compact.

In contrast, for higher AEI contents more Ni agglomerates can be seen. EDX elemental mapping was conducted on the corresponding images of Ni/C cathode catalyst layers, analyzing the distributions of Ni as well as S and Br that are

associated with the Fumion AEI. The results (10 wt% and 40 wt % ionomer content) were compared in Fig. S12. As shown in Fig. S12. a, b, &c, with 10 wt% ionomer content, the Ni distribution is quite uniform and provides the best-performing electrode in this work. On the other hand, an ionomer content of 40 wt% significantly affects the Ni morphology as indicated by a similar distribution pattern to S and Br, in Fig. S12.d, e, &f.

The SEM results of NiO samples with varying ionomer contents are shown in Fig. 10. The SEM images of NiO anode catalytic layers with 5 mg/cm^2 loading show a similar NiO agglomeration morphology for all ionomer contents tested, from 10 wt% to 40 wt%. Note that some charging effects can be seen in Fig. 10.d due to the increased amount of non-conductive ionomer.

Detailed EDX elemental mapping was conducted at the corresponding image sites of NiO anode catalyst layers and the results (10 wt% and 40 wt% ionomer content) were compared in Fig. S13. The comparison shows no significant difference in the Ni distribution (Fig. S13.a & d) when the AEI content was increased from 10 wt% to 40 wt%, which is consistent with the BSE result (Fig. 10). It appears that the NiO morphology is independent of the changing AEI contents.

In conclusion, for the Ni/C cathode, the AEI contents significantly affected the Ni/C morphology and thus potentially resulted in different electrode activity. As ionomer content increases, the agglomeration increases that may cause a loss in three-phase boundary, pore volumes, and the active sites. In contrast, the different AEI contents did not incur much change in NiO morphology, which is consistent with the in-situ half-cell measurements with reference electrodes.

Conclusions

In-situ half-cell measurements with reference electrodes were carried out to identify the influence of anion exchange ionomer (AEI) content on anode and cathode potential contribution. The in-situ half-cell measurements were qualitatively consistent with RDE measurements. Cathode potential was more affected than OER by the AEI content and the optimized AEI content for Ni/C cathode was 10 wt% while NiO anode catalytic layers' potential is independent of the AEI content. The additional overpotential for the cathode one replacing Pt/C with nickel-based catalysts was −295 mV at −10 mA/cm^2 while for the anode one replacing iridium with nickel-based catalysts was 35 mV at 10 mA/cm^2. The largest potential for cost-saving in AEM electrolyzes is therefore associated with the anode since the penalty for replacing iridium with cheaper catalysts is insignificant compared to the penalty for replacing Pt/C. Post-mortem SEM examined the Ni distribution on the surfaces of the cathodes and anodes and compared it with the ionomer distribution. The post-mortem EDX mapping confirmed the presence of Br and S elements from ionomer after electrolysis. The precise tuning of ionomer content for catalysts and AEMWE performance in the presence of supporting electrolytes can reveal many challenges of AEM water electrolysis. Catalyst-ionomer interaction and loading

optimization are essential for further development of AEM water electrolysis.

Declaration of competing interest

The authors declare that they have no known competing financial interests or personal relationships that could have appeared to influence the work reported in this paper.

Acknowledgments

Appendix A. Supplementary data

Supplementary data to this article can be found online at https://doi.org/10.1016/j.ijhydene.2020.07.202.

REFERENCES

[1] International Energy Agency. The future of hydrogen. 2019.
[2] The fuel cells and hydrogen joint undertaking, *hydrogen roadmap Europe: a sustainable pathway for the European energy transition*. 2019.
[3] Faid A, Oyarce Barnett A, Seland F, Sunde S, Faid AY, Oyarce Barnett A, Seland F, Sunde S. Catalysts 2018;8:614.
[4] Carmo M, Fritz DL, Mergel J, Stolten D. Int J Hydrogen Energy 2013;38:4901—34.
[5] Vincent I, Bessarabov D. Renew Sustain Energy Rev 2017:1—15.
[6] Varcoe JR, Atanassov P, Dekel DR, Herring AM, Hickner MA, Kohl PA, Kucernak AR, Mustain WE, Nijmeijer K, Scott K, Xu T, Zhuang L. Energy Environ Sci 2014;7:3135—91.
[7] Vincent I, Kruger A, Bessarabov D. Int J Hydrogen Energy 2017;42:10752—61.
[8] Pushkareva IV, Pushkarev AS, Grigoriev SA, Modisha P, Bessarabov DG. Int J Hydrogen Energy 2019. https://doi.org/10.1016/j.ijhydene.2019.11.011.
[9] Carbone A, Zignani SC, Gatto I, Trocino S, Aricò AS. Int J Hydrogen Energy 2020;45:9285—92.
[10] Park YS, Lee JH, Jang MJ, Jeong J, Park SM, Choi WS, Kim Y, Yang J, Choi SM. Int J Hydrogen Energy 2020;45:36—45.
[11] Zhiani M, Jalili F, Kamali S. Int J Hydrogen Energy 2017;42:26563—74.
[12] Abbasi R, Setzler BP, Lin S, Wang J, Zhao Y, Xu H, Pivovar B, Tian B, Chen X, Wu G, Yan Y. Adv Mater 2019;1805876:1—14.
[13] Jervis R, Mansor N, Sobrido AJ, Jones S, Gibbs C, Neville TP, Millichamp J, Shearing PR, Brett DJL. J Electrochem Soc 2017;164:F1551—5.
[14] Bates MK, Jia Q, Ramaswamy N, Allen RJ, Mukerjee S. J Phys Chem C 2015;119:5467—77.
[15] Li D, Matanovic I, Lee AS, Park EJ, Fujimoto C, Chung HT, Kim YS. ACS Appl Mater Interfaces 2019;11:9696—701.

[16] Alia SM, Pivovar BS. J Electrochem Soc 2018;165:F441—55.

[17] Xu W, Scott K. Int J Hydrogen Energy 2010;35:12029—37.

[18] Roca-Ayats M, Roca-Moreno MD, Martínez-Huerta MV. Int J Hydrogen Energy 2016;41:19656—63.

[19] Kendrick I, Kumari D, Yakaboski A, Dimakis N, Smotkin ES. J Am Chem Soc 2010;132:17611—6.

[20] Li GF, Yang D, Abel Chuang PY. ACS Catal 2018;8:11688—98.

[21] Modestino MA, Kusoglu A, Hexemer A, Weber AZ, Segalman RA. Macromolecules 2012;45:4681—8.

[22] Bernt M, Gasteiger HA. J Electrochem Soc 2016;163:F3179—89.

[23] Kwan JTH, Bonakdarpour A, Afonso G, Wilkinson DP. Electrochim Acta 2017;258:208—19.

[24] Gupta S, Patel MK, Miotello A, Patel N. Adv Funct Mater 2020;30:1906481.

[25] Trotochaud L, Young SL, Ranney JK, Boettcher SW. J Am Chem Soc 2014;136:6744—53.

[26] Jiang Y, Fang Y, Chen C, Ni P, Kong B, Song Z, Lu Y, Niu L. ChemElectroChem 2019;6:3684—9.

[27] Masa J, Sinev I, Mistry H, Ventosa E, de la Mata M, Arbiol J, Muhler M, Roldan Cuenya B, Schuhmann W. Adv Energy Mater 2017;7:1—8.

[28] Chen X, Yu Z, Wei L, Zhou Z, Zhai S, Chen J, Wang Y, Huang Q, Enis Karahan H, Liao X, Chen Y. J Mater Chem A 2019;7:764—74.

[29] Sun H, Xu X, Yan Z, Chen X, Jiao L, Cheng F, Chen J. J Mater Chem A 2018;6:22062—9.

[30] Nsanzimana JMV, Reddu V, Peng Y, Huang Z, Wang C, Wang X. Chem - A Eur J 2018;24:18502—11.

[31] He T, Marie J, Nsanzimana V, Qi R, Zhang JY, Miao M, Yan Y, Qi K, Liu H, Xia BY, Nsanzimana JMV, Qi R, Zhang JY, Miao M, Yan Y, Qi K, Liu H, Xia BY. J Mater Chem A 2018;6:23289—94.

[32] Marie J, Nsanzimana V, Dangol R, Reddu V, Duo S, Peng Y, Dinh KN, Huang Z, Yan Q, Wang X. ACS Appl Mater Interfaces 2018;11:846—55.

[33] Ding R, Liu J, Jiang J, Wu F, Zhu J, Huang X. Catal Sci Technol 2011;1:1406.

[34] Yan H, Zhang D, Xu J, Lu Y, Liu Y, Qiu K, Zhang Y, Luo Y. Nanoscale Res Lett 2014;9:1—7.

[35] Wang Y, Alsmeyer DC, McCreery RL. Chem Mater 1990;2:557—63.

[36] Bin Wu J, Lin ML, Cong X, Liu HN, Tan PH. Chem Soc Rev 2018;47:1822—73.

[37] Mowry M, Palaniuk D, Luhrs CC, Osswald S. RSC Adv 2013;3:21763—75.

[38] Creighton JA, Withnall R. Chem Phys Lett 2000;326:311—3.

[39] Mironova-Ulmane N, Kuzmin A, Steins I, Grabis J, Sildos I, Pärs M. J Phys Conf Ser 2007. https://doi.org/10.1088/1742-6596/93/1/012039.

[40] George G, Anandhan S. RSC Adv 2014;4:62009—20.

[41] Lasia A, Rami A. J Electroanal Chem Interfacial Electrochem 1990;294:123—41.

[42] Faid AY, Barnett AO, Seland F, Sunde S. J Electrochem Soc 2019;166:F519—33.

[43] Li D, Chung HT, Maurya S, Matanovic I, Kim YS. Curr Opin Electrochem 2018;12:189—95.

[44] Matanovic I, Maurya S, Park EJ, Jeon JY, Bae C, Kim YS. Chem Mater 2019;31:4195—204.

[45] Durst J, Siebel A, Simon C, Hasché F, Herranz J, Gasteiger HA. Energy Environ Sci 2014;7:2255—60.

[46] Ernst S, Hamann CH. J Electroanal Chem 1975;60:97—100.